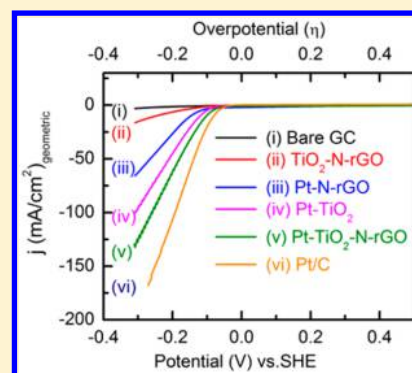


Nitrogen Doped Reduced Graphene Oxide Based Pt–TiO₂ Nanocomposites for Enhanced Hydrogen Evolution

Nitish Roy,[†] Kam Tong Leung,[‡] and Debabrata Pradhan^{*,†}[†]Materials Science Centre, Indian Institute of Technology, Kharagpur 721302, W. B., India[‡]Department of Chemistry, University of Waterloo, Waterloo N2L 3G1, Ontario, Canada**S** Supporting Information

ABSTRACT: Electrochemical hydrogen production from water is an attractive clean energy generation process that has enormous potential for sustainable development. However, noble metal catalysts are most commonly used for such electrochemical hydrogen evolution making the process cost ineffective. Thereby design of hybrid catalysts with minimal use of noble metals using a suitable support material is a prime requirement for the electrolysis of water. Herein, we demonstrate the superior hydrogen evolution reaction (HER) activity of the platinum nanoparticles (Pt NPs) supported on faceted titanium dioxide (TiO₂) nanocrystals (Pt–TiO₂) and nitrogen doped reduced graphene oxide (N-rGO) based TiO₂ nanocomposite (Pt–TiO₂–N-rGO). The ternary Pt–TiO₂–N-rGO nanocomposite exhibits a superior HER activity with a small Tafel slope ($\sim 32 \text{ mV}\cdot\text{dec}^{-1}$), exchange current density ($\sim 0.22 \text{ mA}\cdot\text{cm}^{-2}$), and excellent mass activity ($\sim 3116 \text{ mA}\cdot\text{mg}_{\text{Pt}}^{-1}$) at 300 mV overpotential. These values are better/higher than that of several support materials investigated so far. The excellent HER activity of the ternary Pt–TiO₂–N-rGO nanocomposite is ascribed to the presence of Ti(III) states and enhanced charge transportation properties of N-rGO. The present study is a step toward reliable electrochemical hydrogen production using faceted TiO₂ nanocrystals as support material.



1. INTRODUCTION

Hydrogen evolution from water by means of electrolysis in alkaline or acid media is of great interest due to the present energy crisis. The potential of hydrogen energy lies in its characteristic features of the lightest molecular weight, high diffusion coefficient, highly ignitability, and easily convertibility into electrical or mechanical energy.^{1–3} Platinum (Pt) has so far been recognized as an invincible catalyst for the electrochemical hydrogen evolution reaction (HER). Pt shows promising HER activity with very low overpotential, small Tafel slope ($\sim 30 \text{ mV}\cdot\text{dec}^{-1}$), and high exchange current density ($10^{-3} \text{ A}\cdot\text{cm}^{-2}$).⁴ However, high cost and scarcity of Pt in the Earth's crust limit its large scale applications. In recent years, a few noble metal-free catalysts such as MoS₂, Ni-based alloys, metal pyrites, and graphene/carbon nanotube composites have been employed for HER.^{5–9} Generally, these noble metal-free catalysts are found to exhibit a large overpotential and Tafel slope with a small exchange current density.⁵ In particular, Youn et al. reported graphene-carbon nanotubes supported molybdenum based composites for stable HER with Tafel slope $>50 \text{ mV}\cdot\text{dec}^{-1}$ and exchange current density $\sim 10^{-5} \text{ A}\cdot\text{cm}^{-2}$.¹⁰ Yu et al. showed the layer dependence HER activity of MoS₂ sheets with a Tafel slope $\sim 140 \text{ mV}\cdot\text{dec}^{-1}$ and exchange current density of $\sim 10^{-7} \text{ A}\cdot\text{cm}^{-2}$.¹¹ There are a few more studies on the noble metal-free catalysts for HER but all of those associated with large overpotential and Tafel slope with a low exchange current density ($\sim 10^{-5} \text{ A}\cdot\text{cm}^{-2}$). Although noble metal-free catalysts are highly desirable for cost effectiveness, the large Tafel slope

and small exchange current density make them not suitable for practical applications. Therefore, Pt is indispensable and the most attractive catalyst for HER. Pt shows the smallest Tafel slope ($29 \text{ mV}\cdot\text{dec}^{-1}$), almost zero overpotential, and high exchange current density.⁴ To improve the cost effectiveness of the system, one of the strategies is to reduce the use of Pt content while achieving high exchange current density with small Tafel slope to increase its mass activity. The mass activity of Pt can be enhanced primarily by (a) nanostructuring,¹² (b) making alloys with the non-noble metals,¹³ and (c) depositing the subnanometer size Pt nanoparticles (NPs) on suitable support material.¹⁴ Recently, a few studies have demonstrated enhanced HER mass activity with the noble or rare-earth based metal catalyst supported on oxide.^{15–19} In particular, Khadry et al. reported Pt–SiO₂ nanomaterials with mass activity $11.9 \text{ A}\cdot\text{g}_{\text{Pt}}^{-1}\cdot\text{mV}^{-1}$ (or $11.9 \text{ mA}\cdot\text{mg}_{\text{Pt}}^{-1}\cdot\text{mV}^{-1}$) at overpotential $>250 \text{ mV}$ vs saturated calomel electrode (SCE) in $1 \text{ M H}_2\text{SO}_4$ solution.¹⁵ Zhang et al. reported HER activity of $40 \text{ mA}\cdot\text{cm}^{-2}$ at overpotential 300 mV vs normal hydrogen electrode (NHE) in $0.1 \text{ M H}_2\text{SO}_4$ with Pt–SnO₂ flower-like nanostructures. They also reported a Tafel slope of $111 \text{ mV}\cdot\text{dec}^{-1}$ and exchange current density of $0.46 \text{ mA}\cdot\text{cm}^{-2}$ toward HER.¹⁶ Ham et al. studied the Pt NPs decorated W₂C microspheres which achieved a mass activity of $476 \text{ mA}\cdot\text{mg}_{\text{Pt}}^{-1}$ and current density

Received: April 22, 2015

Revised: June 28, 2015

Published: July 27, 2015

15.8 mA·cm⁻² at 10 mV overpotential vs NHE in 1 M H₂SO₄.¹⁷ They reported the Tafel slope of 103 mV·dec⁻¹ and enhanced exchange current density of 2.08 mA·cm⁻².¹⁷ In the present study, titanium dioxide (TiO₂) is demonstrated as a potential and superior support oxide material for Pt NPs that has shown much higher mass activity than that of recently reported works.^{15–19}

TiO₂ is a well-known self-doped n-type semiconductor catalyst for water splitting reaction whose conduction band (CB) lies just above the HER potential with respect to the standard hydrogen electrode (SHE).^{20–22} The electronic states in TiO₂ can be tuned in various ways such as reducing its surface,^{23,24} changing the stoichiometry,²⁵ doping,²⁶ and/or forming composites.²⁷ Among the different strategies used by researchers to modify the electronic states and thus the properties of TiO₂, reduction has recently attracted enormous attention. This is due to the formation of Ti(III) state, which lowers the CB of Ti(IV) by an extent of ~0.5–1 eV thereby reducing the band gap.^{23,24} Ti(III) state in the reduced TiO₂ is reported to show enhanced visible light photoelectrochemical hydrogen production.^{23,24} In addition, the Ti(III) state in reduced TiO₂ is recently found to exhibit enhanced electrochemical activity toward the electrochemical redox reaction.^{28,29} Taking advantage of the Ti(III) state of reduced TiO₂ near the HER potential, we synthesized reduced Pt–TiO₂ as potential catalyst material for HER. Furthermore, rGO or doped rGO has recently been shown as a promising support material for improved HER performance.^{30–33} Hence, several combinations of Pt, TiO₂, and nitrogen (N) doped hydrothermally reduced graphene oxide (N-hrGO) such as TiO₂ on N-hrGO (TiO₂–N-hrGO), Pt NPs deposited on N-doped reduced graphene oxide (Pt–N-rGO), Pt NPs deposited on TiO₂ NCs (Pt–TiO₂), and Pt NPs deposited on TiO₂–N-hrGO nanocomposite (Pt–TiO₂–N-rGO) hybrid nanomaterials were prepared to study the HER activity. Our findings show an excellent HER performance (very high mass activity, small Tafel slope, and large current density) with ternary Pt–TiO₂–N-rGO nanocomposite suggesting its potential for hydrogen production. The possible mechanism behind the superior electrocatalytic performance of Pt–TiO₂ and Pt–TiO₂–N-rGO nanocomposite is discussed in the present article.

2. EXPERIMENTAL SECTION

Materials. Titanium tetraisopropoxide (TTIP) (99.999%), tetrabutyl ammonium hydroxide (TBAH) [(C₄H₉)₄NOH in 0.1 M aqueous], diethanolamine (DEA), graphite fine powder, potassium permanganate (KMnO₄), sodium borohydride (NaBH₄), sulfuric acid 98% (H₂SO₄), hydrochloric acid 30% (HCl), ethanol (C₂H₅OH), isopropyl alcohol (C₃H₇OH), and hydrogen peroxide 30% (H₂O₂) were purchased from Merck, India. Platinum acetylacetonate [Pt(acac)₂] and 20% Pt/Vulcan (Pt/C) were purchased from Sigma-Aldrich. All the chemicals were used as received.

Synthesis of Graphene Oxide (GO). GO was synthesized by modified Hummers method.³⁴ In a typical synthesis, 2 g of fine graphite powder was added to a concentrated solution of H₂SO₄ (70 mL, 98%), sonicated for 30 min, and stirred at a temperature below 15 °C. Then 6 g of KMnO₄ was added slowly to the reaction mixture, it was heated in an oil bath at 40 °C for 30 min, and 200 mL of water was added. The reaction temperature was then raised to ~80 °C and stirred for another 30 min prior to cooling to room temperature and addition of 500 mL of water. Then ~8 mL of 30% H₂O₂ was added slowly

until the color of the reaction mixture turned yellow from dark brown. After addition of H₂O₂, the reaction mixture was stirred for another 15 min. Then the product was filtered and sequentially washed with DI water, dilute HCl (5%), and DI water. After filtering, the product was dried in vacuum.

In Situ Synthesis of Hydrothermally Reduced Nitrogen Doped GO–TiO₂ (N-hrGO–TiO₂) Nanocomposites. In situ synthesis of N-hrGO–TiO₂ nanocomposite was performed by taking ~20 wt % of as-synthesized dry GO. In a typical synthesis, 40 mg of vacuum-dried GO was dispersed in 40 mL of TBAH and DEA (mol ratio 2:5) mixture and sonicated for 30 min. Then 1 mL of TTIP was added to the above mixture and stirred for a few minutes at room temperature. Then the reaction mixture was transferred into a Teflon-lined stainless steel autoclave and heated at 225 °C for 24 h. After the hydrothermal heat treatment, the autoclave was allowed to cool naturally and the product was collected, washed thoroughly with dilute HCl (5%), water, and ethanol, and finally dried in vacuum.

Synthesis of Hydrothermally Reduced Nitrogen Doped Graphene Oxide (N-hrGO). In order to confirm the N doping in hydrothermal heat treatment of TBAH and DEA with GO, chemically synthesized GO was allowed for hydrothermal heat treatment. In a typical synthesis, 200 mg of GO was added to a mixture of TBAH (20 mL) and DEA (20 mL) and sonicated for 30 min. Then the reaction mixture was transferred into a Teflon-lined stainless steel autoclave and heated at 225 °C for 24 h. After hydrothermal heat treatment, the black colored N-hrGO product was collected and washed in water and isopropyl alcohol. The product was finally dried at 60 °C for 24 h in air.

Deposition of Pt Nanoparticles (NPs) on Cuboid TiO₂ NCs, N-hrGO, and N-hrGO–TiO₂ Nanocomposites. Pt NPs were deposited on the N-hrGO, TiO₂ NCs, or N-hrGO–TiO₂ nanocomposite using Pt(acac)₂ as Pt precursor. Twenty milligrams of TiO₂ or N-hrGO–TiO₂ was taken in 60 mL of water, sonicated for 30 min, and then kept under UV light for 3 h to excite the TiO₂ NCs. Then 30 mL of isopropyl alcohol solution containing 0.5 mg·mL⁻¹ Pt(acac)₂ was added to the TiO₂ or N-hrGO–TiO₂ dispersed solution and stirred for another 1 h under UV light. Then 5 mL of freshly prepared aqueous NaBH₄ solution (5 mg·mL⁻¹) was added to the above reaction mixture. After addition of NaBH₄, the reaction mixture was found to turn black from pearl white (for pristine TiO₂ sample only) indicating the formation of Pt NPs. After 1 h of UV light irradiation, an additional 2 mL of NaBH₄ was added to reduce the partially reduced N-hrGO for the N-hrGO–TiO₂ sample. To deposit Pt on N-hrGO, the reaction mixture was not irradiated under UV light, but 20 mg of N-hrGO was dispersed in 50 mL water and sonicated for 30 min. Then 15 mg of Pt(acac)₂ dissolved in 30 mL of isopropyl alcohol was added with constant stirring. Then 5 mL of freshly prepared NaBH₄ was added and stirred overnight at room temperature to obtain Pt–N-rGO composite.

Characterization. The surface morphology and energy dispersive X-ray (EDX) analysis and microstructure of the products were examined by Carl Zeiss SUPRA field emission scanning electron microscope (FESEM) and TECNAI G2 (FEI) transmission electron microscope (TEM) operated at 200 kV, respectively. The crystallographic phases of the as-synthesized products were obtained by a PANalytical high-resolution powder X-ray diffractometer (HR-XRD) [PW 3040/60] operated at 40 kV and 30 mA using Cu K α X-rays. The

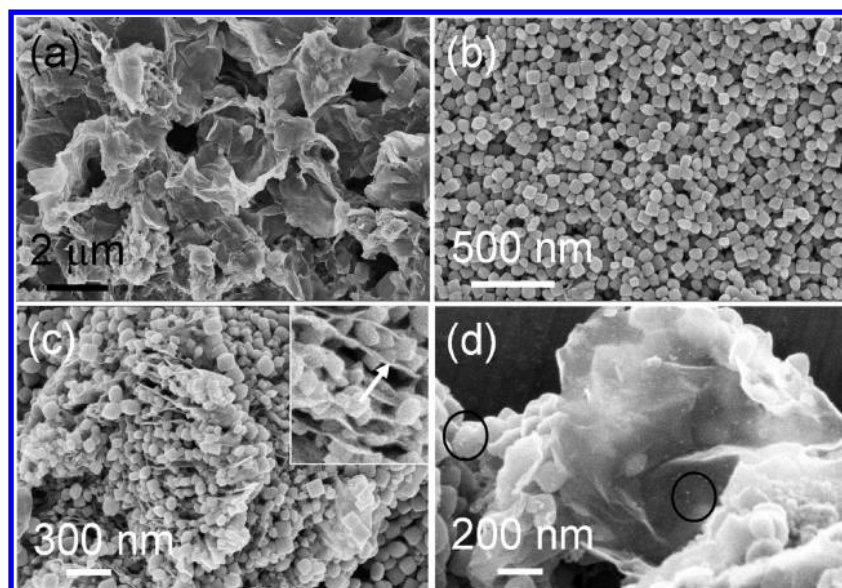


Figure 1. FESEM images of (a) GO, (b) cuboid shaped TiO_2 NCs, (c) TiO_2 -N-hrGO, and (d) Pt- TiO_2 -N-rGO nanocomposites. Inset of (c) shows magnified FESEM image of the corresponding sample showing TiO_2 NCs in between the N-hrGO sheets.

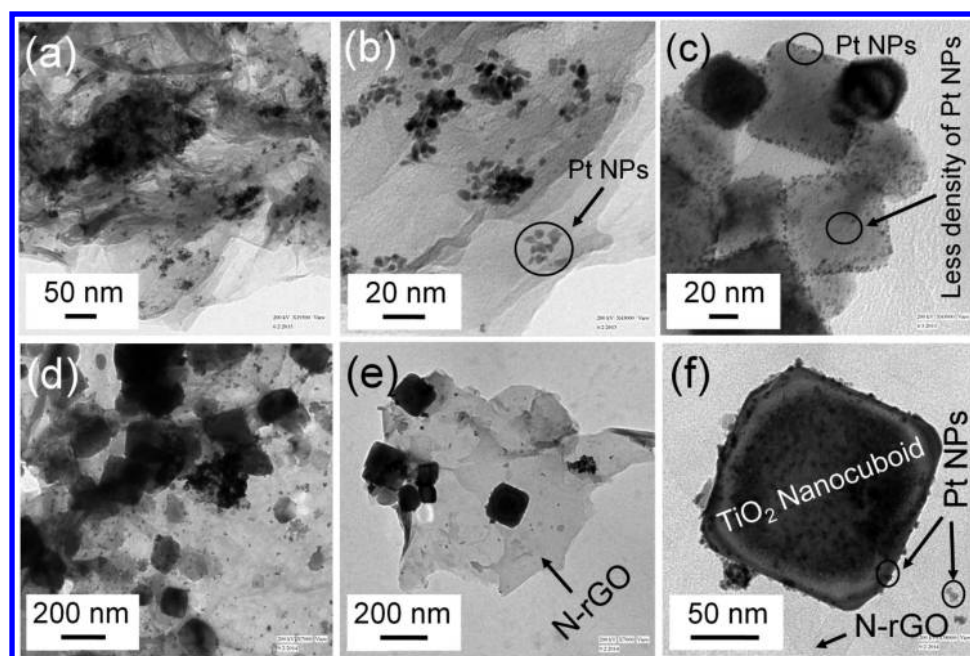


Figure 2. (a, b) TEM images of Pt-N-rGO nanocomposite depicting the sheet structures of N-rGO decorated with chemically reduced Pt NPs. (c) TEM image of Pt- TiO_2 NCs showing the selective photodeposition of <5 nm Pt NPs majorly at the edges of the cuboid shaped TiO_2 NCs. (d, e, f) Ternary nanocomposite of Pt- TiO_2 -N-rGO shows the TiO_2 NCs in between the N-rGO sheets and deposition of Pt NPs on both TiO_2 NCs and N-rGO sheets.

Raman study was carried out with a SENTERRA dispersive Raman microscope (BRUKER) with an excitation wavelength of 532 nm. The XPS measurement was performed by a Thermo-VG Scientific ESCALab 250 microprobe or a PHI 5000 VersaProbe II Scanning XPS Microprobe with a monochromatic Al $K\alpha$ source (1486.6 eV).

Electrochemical Testing. The electrochemical HER activity of the different nanocomposite samples was tested using a CH Instrument (760 D) bipotentiostat with Pt wire as the counter electrode, Ag/AgCl saturated with KCl as the reference electrode, and disc glassy carbon (GC) electrode as the working electrode. Before the catalyst was loaded onto the

disc GC electrode, the electrode surface was washed by sonicating in Millipore water. After the sonochemical cleaning, a slurry of presonicated dispersed catalyst in isopropyl alcohol ($10 \text{ mg}\cdot\text{mL}^{-1}$) was coated onto the GC disc electrode ($50 \mu\text{L}$) by drop casting. The coating was made with care for uniform thickness of the slurry on GC disc and allowed to dry in vacuum overnight. The electrochemical testing was then carried out in a three-electrode system in $0.1 \text{ M H}_2\text{SO}_4$. The scan rate for all the HER activity testing was $100 \text{ mV}\cdot\text{s}^{-1}$ unless mentioned. The potential was calibrated with respect to standard hydrogen electrode (SHE) by adding 0.19 V to the

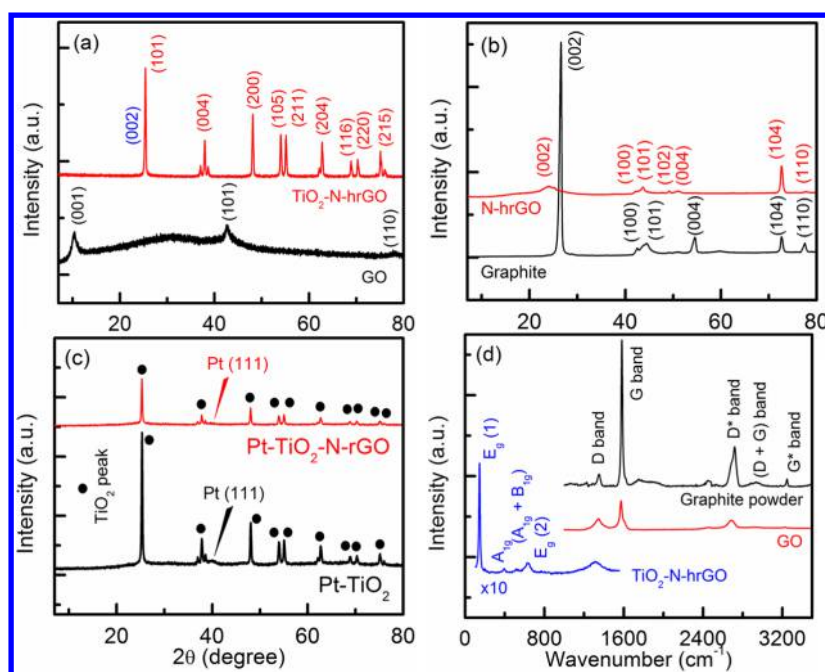


Figure 3. XRD patterns of (a) GO and TiO₂-N-hrGO, (b) graphite and N-hrGO, and (c) Pt-TiO₂ and Pt-TiO₂-N-rGO. (d) Raman spectra of graphite powder, GO, and TiO₂-N-hrGO nanocomposite.

measured potential obtained with KCl saturated Ag/AgCl reference electrode.

3. RESULTS AND DISCUSSION

Morphology. Figure 1 shows the FESEM images of GO, cuboid TiO₂ nanocrystals (NCs), TiO₂-N-hrGO, and Pt-TiO₂-N-rGO nanocomposites. The GO prepared by the modified Hummers method is found to have sheetlike morphology with uniform exfoliation as shown in Figure 1a.³⁴ The length and width of the GO sheets vary in the range 1 μm to a few micrometers. Figure 1b shows an FESEM image of hydrothermally synthesized cuboid faceted anatase TiO₂ NCs with a size range 100–150 nm along the diagonal with uniform surface morphology.³⁵ Figure 1c and 1d show the FESEM images of TiO₂-N-hrGO and Pt-TiO₂-N-rGO nanocomposites, respectively. The TiO₂ NCs are found to be deposited on N-hrGO and also intercalated in between the N-hrGO sheets as clearly observed in the magnified FESEM image shown as the inset of Figure 1c. The arrow in the inset FESEM image of Figure 1c points to N-hrGO sheet. Figure 1d shows that the Pt NPs are deposited not only on N-rGO but also on TiO₂ NCs. The diameter of Pt NPs is found to be extremely small (<5 nm) as marked by the circles in Figure 1d.

TEM analysis was carried out to precisely measure the diameter of Pt NPs and the distribution of the different component in the nanocomposite. Figure 2a and 2b show the TEM images of Pt-N-rGO nanocomposite synthesized by chemical reduction of platinum acetylacetonate [Pt(acac)₂] and N-hrGO. The Pt NPs are found to be nonuniformly deposited on the N-rGO sheets both as individual and as agglomeration. The diameter of individual Pt NPs is measured to be 2–10 nm. On the other hand, much smaller size Pt NPs (<5 nm) are found to deposit at the edges of cuboid TiO₂ NCs by photoreduction under UV light irradiation (Figure 2c) and simultaneous coreduction, i.e., photoreduction and chemical reduction by NaBH₄ (Figure 2d–f) of Pt(acac)₂ on the pristine cuboid TiO₂ NCs without any agglomeration as shown in

Figure 2c–f. A majority of Pt NPs formed by photoreduction are found at the edges of TiO₂ NCs suggesting that the nucleation is facilitated by the edges and due to the reductive {101} facets at the top and bottom 8 edges of TiO₂ cuboids (Figure 2c).³⁵ Figure 2d–f show the TEM images of Pt-TiO₂-N-rGO nanocomposite prepared by simultaneous coreduction, i.e., photoreduction and chemical reduction by NaBH₄ of Pt(acac)₂ and TiO₂-N-hrGO nanocomposite. In this case, Pt NPs are found to be thus deposited on both the N-rGO sheets and cuboid shaped TiO₂ NCs. Although photoreduction facilitates selective deposition at the edges, i.e., on {101} facets, the chemical reduction is nonselective, and therefore Pt NPs are deposited on all the facets of TiO₂ NCs as well as on the N-rGO sheets. The size of the Pt NPs is measured to be in the range of 5–10 nm on the TiO₂ NCs and rGO sheets (Figure 2f).

XRD and Raman Analysis of the Nanocomposites. The phase analysis and conversion of graphite powder to GO were analyzed by XRD and Raman spectroscopy. Figure 3a shows the XRD patterns of GO and in situ hydrothermally synthesized TiO₂-N-hrGO nanocomposite. The diffraction peak at 10.2° in the XRD pattern of GO is assigned to be its intercalated (001) planes.³⁶ In the XRD pattern of TiO₂-N-hrGO, the absence of any Bragg signature in the 2θ region of 10–15° suggests the conversion of GO to N-hrGO upon hydrothermal heat treatment during the TiO₂ NCs synthesis.³⁶ However, a separate peak for N-hrGO at around ~26° is not distinguishable due to the overlap of strong (101) diffraction peak of anatase TiO₂.^{36,37} All the diffraction features in the XRD pattern of TiO₂-N-hrGO nanocomposite is matched with the pure anatase TiO₂.³⁷ This suggests that incorporation of GO in the reaction mixture and subsequent hydrothermal heat treatment do not induce any phase transformation to TiO₂. To confirm the reduction of GO to hrGO via hydrothermal heat treatment, GO synthesized by modified Hummers method was hydrothermally treated with only 0.1 N aqueous tetrabutylammonium hydroxide (TBAH) and dieth-

anolamine (DEA) without using titanium precursor, i.e., titanium tetraisopropoxide (TTIP), and compared with graphite powder (Figure 3b). All the Bragg's diffraction in graphite fine powder is found to match with the JCPDS reference number 00-025-0284 of graphite. The (002) peaks of N-hrGO is found to shift to a lower Bragg's diffraction angle (24.0° compared to 26.8° in the case of graphite powder) clearly indicating the reduction of GO to N-hrGO upon hydrothermal heat treatment. Figure 3c shows the XRD pattern of Pt-TiO₂ and Pt-TiO₂-N-hrGO. A very weak signature at 2θ of 39.6° indicates the Pt(111) peak.³⁸ All other diffraction features match the tetragonal anatase phase of TiO₂ (JCPDS: 00-002-0387). Figure 3d shows the Raman spectra of pure graphite powder, GO, and TiO₂-N-hrGO. The pure graphite powder exhibits strong Raman characteristic G-band at 1580 cm^{-1} and a weak D-band at 1351 cm^{-1} (due to presence of small edge defects in the fine graphite powder).³⁶ The second harmonics of G and D bands are observed at 2717 cm^{-1} (D*), 2937 cm^{-1} (D + G), and 3246 cm^{-1} (G*). The D, G, D*, and G* bands of GO are found to be red-shifted due to the introduction of defects in the exfoliated GO sheets (Table 1).³⁹ These defects

Table 1. Peak Positions of D and G Bands and Their Overtones in the Graphite, GO, and TiO₂-N-hrGO Nanocomposite

| sample | D band (cm ⁻¹) | G band (cm ⁻¹) | D* band (cm ⁻¹) | (D + G) band (cm ⁻¹) | G* band (cm ⁻¹) |
|--------------------------|----------------------------|----------------------------|-----------------------------|----------------------------------|-----------------------------|
| graphite | 1351 | 1580 | 2717 | 2937 | 3246 |
| GO | 1342 | 1571 | 2685 | – | 3224 |
| TiO ₂ -N-hrGO | 1310 | – | – | – | – |

are introduced because of multilayers of GO sheets that can be further analyzed using the intensity ratio of I_G to I_D . The I_G/I_D (2.4) ratio is found to be much lower for GO than that of pure graphite ($I_G/I_D = \sim 13$) revealing the formation of a multilayer GO sheets synthesized via the modified Hummers method. The

D band of N-hrGO in TiO₂-N-hrGO nanocomposite is shifted downward to an extent of 30 cm^{-1} compared to GO (Table 1). This shift could be due to the N doping and/or bonding with TiO₂ NCs which induce strain and defects in N-hrGO.⁴⁰ In addition to imposed defects and strain by doping, this red shift could also be ascribed to the downward shift of Fermi level (E_F) of N-hrGO as compared to GO.^{40,41} The different Raman modes of TiO₂ are assigned for TiO₂-N-hrGO in Figure 3d. All the Raman modes of TiO₂ in TiO₂-N-hrGO are found to shift $\pm 5\text{ cm}^{-1}$ compared to the reported values; e.g., $E_g(1)$ peak shifts from 141 to 145 cm^{-1} , $E_g(2)$ peak shifts from 637 to 632 cm^{-1} , A_{1g} peak shifts from 397 to 394 cm^{-1} , and ($A_{1g} + B_{1g}$) peak shifts from 514 to 520 cm^{-1} .

Surface Composition of the Nanocomposites. X-ray photoelectron spectroscopy (XPS) is employed to measure the surface composition and chemical states of the element present and the nature of bonding in the as-synthesized nanocomposites. Figure S1 in the Supporting Information shows the survey spectra of pristine TiO₂, Pt-TiO₂, Pt-TiO₂-N-rGO, and TiO₂-N-hrGO samples. The binding energy (BE) of photoelectron peaks were calibrated with C 1s peak at 284.5 eV . In addition to the expected elements present, the samples containing rGO show N 1s XPS peak (Figure S2) indicating the N-doping/bonding in rGO. It is to be noted that DEA and TBAH were used in the synthesis of TiO₂-based rGO nanocomposites (TiO₂-N-hrGO and Pt-TiO₂-N-rGO). It is known that hydrothermal heat treatment reduces the GO to rGO which is also confirmed by XRD analysis (Figure 3b) in the present work.⁴² Although nitrogen is not doped in TiO₂ NCs, it can be doped into the GO sheets upon hydrothermal heat treatment.^{35,43} In order to confirm the N-doping in GO containing nanocomposites, XPS analysis was carried out on the N-hrGO and compared with GO as shown in Figure S3. Part (a) of Figure S3 shows the XPS survey spectra of GO and hydrothermally treated GO, i.e., N-hrGO. The atomic % of oxygen is found to decrease from 29% (for GO) to 23% (for N-hrGO) suggesting that hydrothermal heat treatment leads to

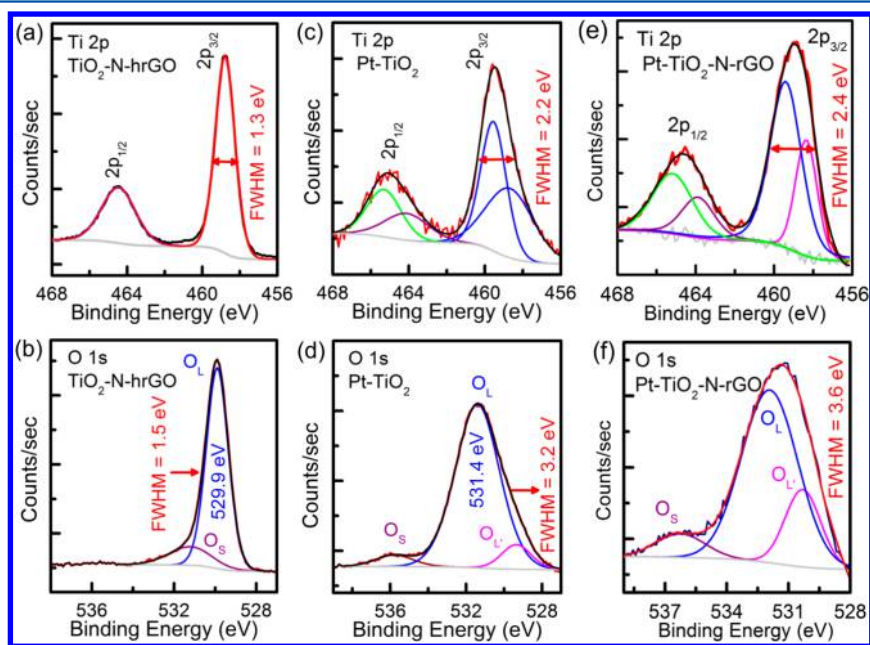


Figure 4. (a, c, e) Ti 2p and (b, d, f) O 1s region XPS spectra of (a, b) TiO₂-N-hrGO, (c, d) Pt-TiO₂, and (e, f) Pt-TiO₂-N-rGO nanocomposites.

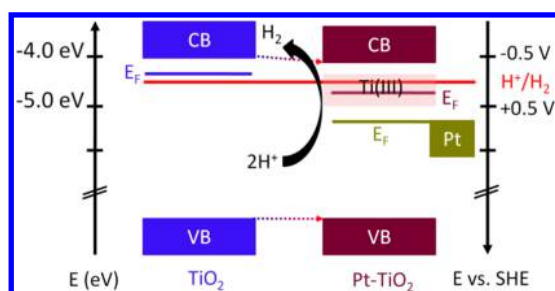
partial reduction of GO to N-hrGO which is in accord with the XRD analysis (Figure S3a and Figure 3b). In addition, N-doping occurs as revealed by the presence of N 1s photoelectron peak in the surface survey of N-hrGO (Figure S3a). The details on the type of bonding are further confirmed by the C 1s and N 1s XPS region spectra (Figure S3b–d).⁴⁴ Parts (b) and (c) of Figure S3 in the Supporting Information show the C 1s region spectra of GO and N-hrGO, respectively. The C 1s of GO shows two different distinct photoelectron peaks at 284.5 eV (C-1) and 286.7 eV (C-3), which can be assigned to the C–C sp² photoelectron and C–O/C=O and/or O=C=O photoelectron peaks, respectively. The deconvolution of C 1s of N-hrGO exhibits three different photoelectron features which are assigned to C–C at 284.5 eV (C-1), C–N/C–O at 285.9 eV (C-2), and C=O/O=C=O at 286.5 eV (C-3).⁴⁴ Similarly, deconvoluted N 1s region spectra shows three different photoelectron peaks at 399.1, 399.8, and 401.3 eV in N-hrGO, which are assigned to pyridinic-N (N-6), pyrrolic-N (N-5), and quaternary-N (N-Q), respectively (Figure S3d).^{44,45}

Figure 4a, c, e and 4b, d, f show the XPS region spectra of Ti 2p and O 1s, respectively, in TiO₂–N-hrGO, Pt–TiO₂, and Pt–TiO₂–N-rGO nanocomposites. The BE of Ti 2p photoelectron peaks in TiO₂–N-hrGO nanocomposite is found to be symmetric and at 458.9 eV (2p_{3/2}) and 464.6 eV (2p_{1/2}) confirming the Ti(IV) state (Figure 4a).^{46,47} However, Ti 2p of Pt–TiO₂ and Pt–TiO₂–N-rGO nanocomposites is found to be broader [full width at half-maximum (fwhm) of Ti 2p_{3/2} peak is 2.2 and 2.4 eV, respectively] than that of Ti 2p of TiO₂–N-hrGO nanocomposite (fwhm is 1.3 eV) (Figure 4a, c, e). Due to the nonsymmetric nature of Ti 2p feature of Pt–TiO₂ and Pt–TiO₂–N-rGO nanocomposites, it is deconvoluted as shown in Figure 4c, e. The BE at 459.6 and 465.2 eV are assigned to the 2p_{3/2} and 2p_{1/2} peaks of Ti(IV) states, while the photoelectron peaks at 458.7 and 464.2 eV can be assigned to the 2p_{3/2} and 2p_{1/2} peaks of Ti(III) in Pt–TiO₂ nanocomposite (Figure 4c).⁴⁷ It should also be noted that the Ti 2p photoelectron peaks of Ti(IV) in Pt–TiO₂ nanocomposite are found at higher BE than that of Ti 2p peaks of Ti(IV) state in TiO₂–N-hrGO nanocomposite (2p_{3/2} = 458.9 and 2p_{1/2} = 464.6 eV). Similarly, BE at 459.5 and 465.2 eV reveals the Ti(IV) state, and 458.3 and 463.9 eV reveals the Ti(III) state of the sample Pt–TiO₂–N-rGO nanocomposite. The higher BE of 2p electrons of Ti(IV) in Pt–TiO₂ nanocomposite is due to the positive shift of E_F (or away from vacuum level) as shown in Scheme 1 that can be described on the basis of formation of nonstoichiometric TiO_x in Pt–TiO₂.²⁷ It is important to note that E_F shifts to negative potential for the stoichiometric TiO₂ and metal nanoparticle

composite.^{48,49} The positive shift of E_F in the present study resulted in the increase in BE of the Ti(IV) photoelectron peaks in Pt–TiO₂ and Pt–TiO₂–N-rGO nanocomposites compared to TiO₂–N-hrGO (Figure 4, Scheme 1). The lattice O 1s peaks (O_L) of Pt–TiO₂ and Pt–TiO₂–N-rGO nanocomposites are also found at higher BE (531.4 and 531.9 eV, respectively) than that of O_L (529.9) of TiO₂–N-hrGO which is due to the similar reason (positive E_F shifting in Pt–TiO₂, Scheme 1 and Figure 4b, d, f). The two O 1s (O_L and O_{L'}) features for Pt–TiO₂ and Pt–TiO₂–N-rGO nanocomposites are due to the lattice O²⁻ bonded with Ti(IV) and Ti(III) states, respectively. The relative population of O_{L'} feature in the Pt–TiO₂–N-rGO nanocomposite is measured to be ~3 times higher than the Pt–TiO₂ nanocomposite. The O_S peaks of Pt–TiO₂ and Pt–TiO₂–N-rGO nanocomposites (Figure 4b, d) are found to be at ~536 eV which is much higher than the O_S peak of TiO₂–N-hrGO (Figure 4f). In addition, the relative population of Ti(III) state is estimated to increase by ~1.5 times for Pt–TiO₂–N-rGO compared to that of Pt–TiO₂ which is in accord with the increase in O_{L'} feature of the corresponding samples (Figure 4e, f). The increase of Ti(III) state in Pt–TiO₂–N-rGO nanocomposite compared to Pt–TiO₂ is due to the excess use of NaBH₄ during the deposition of Pt NPs for the synthesis of Pt–TiO₂–N-rGO. The reduction of TiO₂ surface is ascribed to the fact that the excited TiO₂ NC's surface could take up electrons from the reducing agent (NaBH₄) thereby reducing the surface Ti(IV) to Ti(III) states of TiO₂. Figure S4 shows the XPS spectra of Pt 4f photoelectron peaks of Pt–TiO₂ and Pt–TiO₂–N-rGO nanocomposites. The BE of Pt 4f peaks are well matched with the reported values with a spin orbit splitting of ~3.3 eV in both the Pt–TiO₂ and Pt–TiO₂–N-rGO nanocomposites.^{48,49}

HER Activity. HER activity of the as-synthesized samples was tested in 0.1 M H₂SO₄ at a scan rate 100 mV·s⁻¹. Figure 5a shows the linear sweep voltammograms (LSVs) presenting the current density as a function of applied potential (vs. SHE) and overpotential (η) for different catalyst samples. As these composite catalysts were coated on the glassy carbon (GC) electrode by drop casting, the HER activity was also measured with bare GC for comparison. It is found that the ternary Pt–TiO₂–N-rGO nanocomposite exhibits a maximum current density of 126 mA·cm⁻² at an overpotential of 300 mV. Overall the Pt-based catalysts exhibit higher current density than TiO₂–N-rGO as expected. Figure 5b shows the Tafel plots in the linear portion of HER. The average Tafel slopes for Pt–N-rGO, Pt–TiO₂, Pt–TiO₂–N-rGO, and Pt/C nanocomposites are measured (from the linear portion of Figure 5b) to be in the range 29–32 mV·dec⁻¹, i.e., the potential required to increase the current density 10 times. The Tafel slope value suggests information about the HER mechanism.⁵ The slope in the range of ~29 mV·dec⁻¹ and 38–42 mV·dec⁻¹ were reported to follow the atom combination and atom ion combination mechanism for HER, respectively.⁵ The smaller slopes (29–32 mV·dec⁻¹) obtained with Pt/C, Pt–N-rGO, Pt–TiO₂, and Pt–TiO₂–N-rGO nanocomposites in the present work suggest that these catalysts follow an atom combination mechanism.⁵ The ternary Pt–TiO₂–N-rGO nanocomposite exhibits the exchange current density of 0.22 mA·cm⁻² while Pt–TiO₂ and Pt–N-rGO exhibit exchange current density of 0.19 mA·cm⁻² and 0.38 mA·cm⁻², respectively (exchange current densities were measured by the intercepts of X-axis of the inverse slope of Tafel plots). Furthermore, the mass activity of Pt–TiO₂–N-rGO nanocomposite is estimated to be the highest (3116 mA·

Scheme 1. Electronic Band Positions of Ti(III) in Pt–TiO₂ Based Nanocomposite



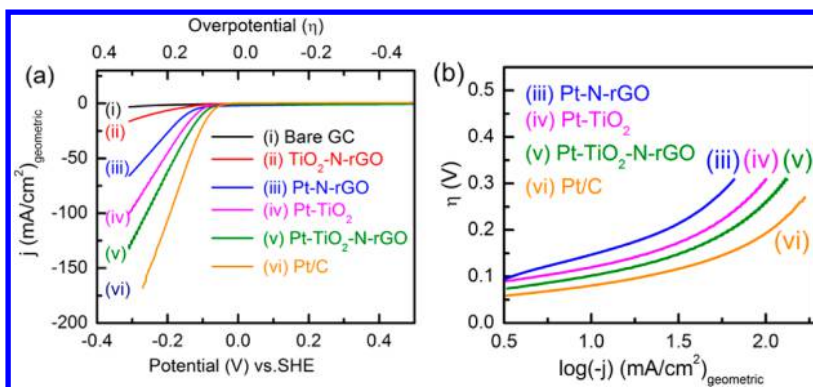


Figure 5. (a) HER activity of the different nanocomposite catalysts in 0.1 N H₂SO₄ at a scan rate of 100 mV·s⁻¹. (b) Tafel plot of the different Pt-based nanocomposites. The current density was measured considering the geometric area of the working disc GC electrode.

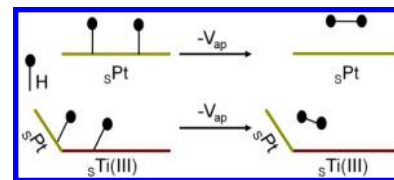
Table 2. Tafel Slope (*b*), Exchange Current Density (*j*₀), Current Density (*j*), and Mass Activity of the Pt-Based Catalysts

| catalyst | <i>b</i> (mV·dec ⁻¹) | <i>j</i> ₀ (mA·cm ⁻²) | <i>j</i> (mA·cm ⁻²) | <i>η</i> (mV) | mass activity (mA·mg _{Pt} ⁻¹) |
|----------------------------|----------------------------------|--|---------------------------------|---------------|--|
| Pt–TiO ₂ –N–rGO | 32 | 0.22 | 126 | 300 | 3110 |
| Pt–TiO ₂ | 32 | 0.19 | 97 | 300 | 2059 |
| Pt–N–rGO | 37 | 0.38 | 65 | 300 | 1491 |
| Pt/C | 29 | 24 | 171 | 300 | 1338 |

mg⁻¹) among all the catalysts synthesized in the present work at an overpotential of 300 mV. In order to estimate the mass activity, the wt % of Pt in the as-synthesized samples was first measured using EDX. The Pt wt % in Pt–TiO₂–N–rGO, Pt–TiO₂, and Pt–N–rGO were measured to be 6.33%, 7.36%, and 6.84%, respectively (Figure S5). The mass loadings of the corresponding samples are estimated to be 2.83, 3.2, and 3.05 μg while the mass loading of 20 wt % Pt/C is 8.94 μg. The Tafel slope, current density, mass activity, and exchange current density of the as-synthesized Pt-based catalysts are summarized in Table 2 and compared with 20 wt % Pt on Vulcan carbon (Pt/C). The scan rate dependent HER activity and stability of the ternary Pt–TiO₂–N–rGO nanocomposite are shown in Figures S6 and S7, respectively. It is found that the current density decreases from 126 to 115 mA·cm⁻² upon decrease in scan rate from 100 to 50 mV·s⁻¹. The ternary Pt–TiO₂–N–rGO nanocomposite is found to be stable even in 100th run. After a 100th cycle, the overpotential is found to increase by 1.2 mV at current density of 86 mA·cm⁻² (Figure S7).

The HER mechanism here involves two steps: (1) adsorption of proton on the catalytically active sites of the electrode coupled with an electron transfer and (2) desorption of two adsorbed protons to produce hydrogen gas.^{5,32} This atom combination HER mechanism (or Volmer–Tafel mechanism), which proceeds through the above two steps, is illustrated in Scheme 2. The proton-couple electron transfer is reported to occur on reduced TiO₂ surface.^{50–52} Furthermore, the Ti(III) states are known to be electrochemically active and decrease the overpotential for the electrochemical reduction by effective electron transfer from the Ti(III) states.²⁸ XPS analysis in the present study reveals the presence of the Ti(III) state in Pt–TiO₂ and Pt–TiO₂–N–rGO nanocomposites. The Ti(III) state on the electrode surface is thus attributed to higher HER activity of ternary Pt–TiO₂–N–rGO and Pt–TiO₂ than that of Pt–N–rGO nanocomposite (Table 2). It is also important to note that the Ti(III) states not only increase the n-doping degree of TiO₂ and thus improve the conductivity but also increase the protonation that facilitates the HER as shown in

Scheme 2. Atom Combination of HER Mechanism on Pt and Pt–TiO₂ Surface^a



^aSubscript 's' denotes the surface of the respective surface; Ti(III) only indicates the reduced state of the TiO₂ in the composites. *V*_{ap} is the applied potential in HER.

Scheme 2.^{28,53,54} The superior HER activity of the Pt–TiO₂–N–rGO in spite of the larger size of Pt NPs (5–10 nm) compared to Pt NPs (2–5 nm) on Pt–TiO₂ can be attributed to following two major factors: (i) increase in the Ti(III) states by an extent of 33% for Pt–TiO₂–N–rGO as compared to Pt–TiO₂ as confirmed by XPS analysis and (ii) the enhanced charge transportation due to the presence of N–rGO in the Pt–TiO₂–N–rGO nanocomposite.⁵⁵ In addition, the HER activity of the Pt–N–rGO is found to be slightly higher than the Pt–rGO composite (not shown). This suggests the higher electrical conductivity and active sites for HER in Pt–N–rGO due to N-doping, which can be considered as another factor for enhanced HER activity. The HER activity of as-synthesized catalysts is compared with the literature values and presented in Table 3.

4. CONCLUSIONS

In this study, we demonstrate the synthesis of TiO₂-based nanocomposite catalysts with different combination of TiO₂ NCs, N–rGO, and Pt NPs for HER. The Pt NPs deposited on TiO₂ NCs by photoreduction are smaller and more uniform than that deposited on GO by chemical reduction. The ternary Pt–TiO₂–N–rGO nanocomposite exhibits a maximum current density (126 mA·cm⁻² at 300 mV overpotential) with a small Tafel slope (~32 mV·dec⁻¹), high mass activity (3116 mA·mg_{Pt}⁻¹), and high exchange current density (0.22 mA·cm⁻²). The small Tafel slope indicates that the HER mechanism

Table 3. Comparison of HER Current Density (j), Exchange Current Density (j_0), Tafel Slope (b), and Mass Activity with the Reported Catalysts

| catalyst | η (mV) | j (mA·cm ⁻²) | b (mV·dec ⁻¹) | j_0 (mA·cm ⁻²) | scan rate (mV·s ⁻¹) | electrolyte | mass activity (mA·mg ⁻¹) | ref |
|----------------------------------|------------------|----------------------------|-----------------------------|------------------------------|---------------------------------|--------------------------------------|--------------------------------------|-----------|
| Pt–TiO ₂ | 300 | 97 | 32 | 0.19 | 100 | 0.1 M H ₂ SO ₄ | 2059 | this work |
| Pt–TiO ₂ –N-rGO | 300 | 126 | 32 | 0.22 | 100 | 0.1 M H ₂ SO ₄ | 3116 | this work |
| Pt–SiO ₂ | 500 ^a | 200 | – | – | 50 | 1 M H ₂ SO ₄ | – | ref15 |
| Pt–SnO ₂ | 300 | 40 | 111 | 0.46 | 10 | 0.1 M H ₂ SO ₄ | – | ref16 |
| Pt foil | 10 | 14 | 108 | 1.8 | 2 | 1 M H ₂ SO ₄ | 0.91 | ref17 |
| Pt–W ₂ C | 10 | 15.8 | 103 | 2 | 2 | 1 M H ₂ SO ₄ | 476 | ref17 |
| Cu _x –Pt _y | 800 | 5 | – | – | 100 | phosphate buffer (pH 7) | 275 | ref19 |

^a η vs. SCE.

follows the atom combination discharge process. The excellent electrocatalytic behavior of ternary Pt–TiO₂–N-rGO nanocomposite toward HER is attributed to the synergistic effect of Ti(III) state of reduced TiO₂ NCs and N-rGO with Pt NPs. The Ti(III) state enhances the hydrogen discharge process and N-rGO facilitates the charge transfer from electrode to catalyst surface which lead to increase in the HER activity. The present study is an attempt toward reducing the Pt content and demonstrating TiO₂ as a suitable inexpensive support oxide material for the production of hydrogen energy.

■ ASSOCIATED CONTENT

Supporting Information

The Supporting Information is available free of charge on the ACS Publications website at DOI: 10.1021/acs.jpcc.5b03870.

XPS surface survey, region spectra, EDX spectra, and cyclic voltammograms for HER (PDF)

■ AUTHOR INFORMATION

Corresponding Author

*Phone: +91 3222 281798. Fax: +91 3222 282274. E-mail: deb@matsc.iitkgp.ernet.in.

Notes

The authors declare no competing financial interest.

■ ACKNOWLEDGMENTS

This work was supported by Science and Engineering Research Board (SERB), New Delhi, India through the grant SB/S1/IC-15/2013. N.R. is thankful to CSIR New Delhi, India for financial support. K.T.L. is grateful for the support of the Natural Sciences and Engineering Research Council of Canada.

■ REFERENCES

- (1) Midilli, A.; Ay, M.; Dincer, I.; Rosen, M. A. On Hydrogen and Hydrogen Energy Strategies I: Current Status and Needs. *Renewable Sustainable Energy Rev.* **2005**, *9*, 255–271.
- (2) Jamal, Y.; Wyszynski, M. L. On-board Generation of Hydrogen-Rich Gaseous Fuels—A Review. *Int. J. Hydrogen Energy* **1994**, *19*, 557–572.
- (3) Momirlan, M.; Veziroglu, T. N. Current Status of Hydrogen Energy. *Renewable Sustainable Energy Rev.* **2002**, *6*, 141–179.
- (4) Sheng, W.; Gasteiger, H. A.; Shao-Horn, Y. Hydrogen Oxidation and Evolution Reaction Kinetics on Platinum: Acid vs. Alkaline Electrolytes. *J. Electrochem. Soc.* **2010**, *157*, B1529–B1536.
- (5) Morales-Guio, C. J.; Stern, L.-A.; Hu, X. Nanostructured Hydrotreating Catalysts for Electrochemical Hydrogen Evolution. *Chem. Soc. Rev.* **2014**, *43*, 6555–6569.

(6) Lupi, C.; Dell’Era, A.; Pasquali, M. In Situ Activation with Mo of NiCo Alloys for Hydrogen Evolution Reaction. *Int. J. Hydrogen Energy* **2014**, *39*, 1932–1940.

(7) Lupi, C.; Dell’Era, A.; Pasquali, M. Nickel–Cobalt Electrodeposited Alloys for Hydrogen Evolution in Alkaline Media. *Int. J. Hydrogen Energy* **2009**, *34*, 2101–2106.

(8) Faber, M. S.; Lukowski, M. A.; Ding, Q.; Kaiser, N. S.; Jin, S. Earth-Abundant Metal Pyrites (FeS₂, CoS₂, NiS₂, and Their Alloys) for Highly Efficient Hydrogen Evolution and Polysulfide Reduction Electrocatalysis. *J. Phys. Chem. C* **2014**, *118*, 21347–21356.

(9) Cui, W.; Liu, Q.; Cheng, N.; Asiri, A. M.; Sun, X. Activated Carbon Nanotubes: A Highly-Active Metal-free Electrocatalyst for Hydrogen Evolution Reaction. *Chem. Commun.* **2014**, *50*, 9340–9342.

(10) Youn, D. H.; Han, S.; Kim, J. Y.; Kim, J. Y.; Park, H.; Choi, S. H.; Lee, J. S. Highly Active and Stable Hydrogen Evolution Electrocatalysts Based on Molybdenum Compounds on Carbon Nanotube–Graphene Hybrid Support. *ACS Nano* **2014**, *8*, 5164–5173.

(11) Yu, Y.; Huang, S. Y.; Li, Y.; Steinmann, S. N.; Yang, W.; Cao, L. Layer-Dependent Electrocatalysis of MoS₂ for Hydrogen Evolution. *Nano Lett.* **2014**, *14*, 553–558.

(12) Chen, S.; Kucernak, A. Electrocatalysis under Conditions of High Mass Transport: Investigation of Hydrogen Oxidation on Single Submicron Pt Particles Supported on Carbon. *J. Phys. Chem. B* **2004**, *108*, 13984–13994.

(13) Cao, X.; Han, Y.; Gao, C.; Xu, Y.; Huang, X.; Willander, M.; Wang, N. Highly Catalytic Active PtNiCu Nanochains for Hydrogen Evolution Reaction. *Nano Energy* **2014**, *9*, 301–308.

(14) Huang, H.; Leung, D. Y. C.; Ye, D. Effect of Reduction Treatment on Structural Properties of TiO₂ Supported Pt Nanoparticles and Their Catalytic Activity for Formaldehyde Oxidation. *J. Mater. Chem.* **2011**, *21*, 9647–9652.

(15) Khadry, N. H.; Ghanem, M. A. Highly Dispersed Platinum Nanoparticles Supported on Silica as Catalyst for Hydrogen Production. *RSC Adv.* **2014**, *4*, 50114–50122.

(16) Zhang, H.; Hu, C.; Chen, S.; Zhang, K.; Wang, X. Synthesis of SnO₂ Nanostructures and Their Application for Hydrogen Evolution Reaction. *Catal. Lett.* **2012**, *142*, 809–815.

(17) Ham, D. J.; Ganesan, R.; Lee, J. S. Tungsten Carbide Microsphere as an Electrode for Cathodic Hydrogen Evolution from Water. *Int. J. Hydrogen Energy* **2008**, *33*, 6865–6872.

(18) Kuttiviyl, K. A.; Sasaki, K.; Chen, W.-F.; Su, D.; Adzic, R. R. Core–shell, Hollow-Structured Iridium–Nickel Nitride Nanoparticles for the Hydrogen Evolution Reaction. *J. Mater. Chem. A* **2014**, *2*, 591–594.

(19) Chen, Z.; Ye, S.; Wilson, A. R.; Ha, Y.-C.; Wiley, B. J. Optically Transparent Hydrogen Evolution Catalysts Made from Networks of Copper–Platinum Core–Shell Nanowires. *Energy Environ. Sci.* **2014**, *7*, 1461–1467.

(20) Beranek, R. (Photo)electrochemical Methods for the Determination of the Band Edge Positions of TiO₂-Based Nanomaterials. *Adv. Phys. Chem.* **2011**, *1*–20.

(21) Park, J. T.; Roh, D. K.; Patel, R.; Kim, E.; Ryu, D. Y.; Kim, J. H. Preparation of TiO₂ Spheres with Hierarchical Pores via Grafting

Polymerization and Sol–Gel Process for Dye-Sensitized Solar Cells. *J. Mater. Chem.* **2010**, *20*, 8521–8530.

(22) Trasatti, S. The Absolute Electrode Potential: An Explanatory Note. *Pure Appl. Chem.* **1986**, *58*, 95–96.

(23) Wang, Z.; Yang, C.; Lin, T.; Yin, H.; Chen, P.; Wan, D.; Xu, F.; Huang, F.; Lin, J.; Xie, X.; et al. H-Doped Black Titania with Very High Solar Absorption and Excellent Photocatalysis Enhanced by Localized Surface Plasmon Resonance. *Adv. Funct. Mater.* **2013**, *23*, 5444–5450.

(24) Chen, X.; Liu, L.; Yu, P. Y.; Mao, S. S. Increasing Solar Absorption for Photocatalysis with Black Hydrogenated Titanium Dioxide Nanocrystals. *Science* **2011**, *331*, 746–750.

(25) Wang, S.; Pan, L.; Song, J.-J.; Mi, W.; Zou, J.-J.; Wang, L.; Zhang, X. Titanium-Defected Undoped Anatase TiO₂ with p-Type Conductivity, Room-Temperature Ferromagnetism, and Remarkable Photocatalytic Performance. *J. Am. Chem. Soc.* **2015**, *137*, 2975–2983.

(26) Roy, N.; Sohn, Y.; Leung, K. T.; Pradhan, D. Engineered Electronic States of Transition Metal Doped TiO₂ Nanocrystals for Low Overpotential Oxygen Evolution Reaction. *J. Phys. Chem. C* **2014**, *118*, 29499–29506.

(27) Shi, F.; Baker, L. R.; Hervier, A.; Somorjai, J. A.; Komvopoulos, K. Tuning the Electronic Structure of Titanium Oxide Support to Enhance the Electrochemical Activity of Platinum Nanoparticles. *Nano Lett.* **2013**, *13*, 4469–4474.

(28) Ramesha, G. K.; Brennecke, J. F.; Kamat, P. V. Origin of Catalytic Effect in the Reduction of CO₂ at Nanostructured TiO₂ Films. *ACS Catal.* **2014**, *4*, 3249–3254.

(29) Chang, X.; Thind, S. S.; Chen, A. Electrocatalytic Enhancement of Salicylic Acid Oxidation at Electrochemically Reduced TiO₂ Nanotubes. *ACS Catal.* **2014**, *4*, 2616–2622.

(30) Wang, H.; Maiyalagan, T.; Wang, X. Review on Recent Progress in Nitrogen-Doped Graphene: Synthesis, Characterization, and Its Potential Applications. *ACS Catal.* **2012**, *2*, 781–794.

(31) Das, R. K.; Wang, Y.; Vasilyeva, S. V.; Donoghue, E.; Pucher, I.; Kamenov, G.; Cheng, H.-P.; Rinzler, A. G. Extraordinary Hydrogen Evolution and Oxidation Reaction Activity from Carbon Nanotubes and Graphitic Carbons. *ACS Nano* **2014**, *8*, 8447–8456.

(32) Li, Y.; Wang, H.; Xie, L.; Liang, Y.; Hong, G.; Dai, H. MoS₂ Nanoparticles Grown on Graphene: An Advanced Catalyst for the Hydrogen Evolution Reaction. *J. Am. Chem. Soc.* **2011**, *133*, 7296–7299.

(33) Tang, H.; Dou, K.; Kaun, C.-C.; Kuang, Q.; Yang, S. MoSe₂ Nanosheets and their Graphene Hybrids: Synthesis, Characterization and Hydrogen Evolution Reaction Studies. *J. Mater. Chem. A* **2014**, *2*, 360–364.

(34) Hummers, W. S.; Offeman, R. E. Preparation of Graphitic Oxide. *J. Am. Chem. Soc.* **1958**, *80*, 1339–1339.

(35) Roy, N.; Sohn, Y.; Pradhan, D. Synergy of Low-Energy {101} and High-Energy {001} TiO₂ Crystal Facets for Enhanced Photocatalysis. *ACS Nano* **2013**, *7*, 2532–2540.

(36) Mhamane, D.; Ramadan, W.; Fawzy, M.; Rana, A.; Dubey, M.; Rode, C.; Lefez, B.; Hannoyer, B.; Ogale, S. From Graphite Oxide to Highly Water Dispersible Functionalized Graphene by Single Step Plant Extract-Induced Deoxygenation. *Green Chem.* **2011**, *13*, 1990–1996.

(37) Roy, N.; Park, Y.; Sohn, Y.; Leung, K. T.; Pradhan, D. Green Synthesis of Anatase TiO₂ Nanocrystals with Diverse Shapes and their Exposed Facets Dependent Photoredox Activity. *ACS Appl. Mater. Interfaces* **2014**, *6*, 16498–16507.

(38) Garcia, R. M.; Song, Y.; Dorin, R. M.; Wang, H.; Moreno, A. M.; Jiang, Y.-B.; Tian, Y.; Qiu, Y.; Medforth, C. J.; Coker, E. N.; et al. Templated Growth of Platinum Nanowheels Using the Inhomogeneous Reaction Environment of Bicelles. *Phys. Chem. Chem. Phys.* **2011**, *13*, 4846–4852.

(39) Guo, B.; Liu, Q.; Chen, E.; Zhu, H.; Fang, L.; Gong, J. R. Controllable N-Doping of Graphene. *Nano Lett.* **2010**, *10*, 4975–4980.

(40) Lv, R.; Li, Q.; Botello-Mendez, A. R.; Hayashi, T.; Wang, B.; Berkdemir, A.; Hao, Q.; Elias, A. L.; Cruz-Silva, R.; Gutierrez, H. R.;

Kim, Y. A.; Muramatsu, H.; Zhu, J.; Endo, M.; Terrones, H.; Charlier, J.-C.; Pan, M.; Terrones, M.; et al. Nitrogen-Doped Graphene: Beyond Single Substitution and Enhanced Molecular Sensing. *Sci. Rep.* **2012**, *2*, 586.

(41) Das, A.; Pisana, S.; Chakraborty, B.; Piscanec, S.; Saha, S. K.; Waghmare, U. V.; Novoselov, K. S.; Krishnamurthy, H. R.; Geim, A. K.; Ferrari, A. C.; Sood, A. K.; et al. Monitoring Dopants by Raman Scattering in an Electrochemically Top-Gated Graphene Transistor. *Nat. Nanotechnol.* **2008**, *3*, 210–215.

(42) Zhou, Y.; Bao, Q.; Tang, L. A. L.; Zhong, Y.; Loh, K. P. Hydrothermal Dehydration for the “Green” Reduction of Exfoliated Graphene Oxide to Graphene and Demonstration of Tunable Optical Limiting Properties. *Chem. Mater.* **2009**, *21*, 2950–2956.

(43) Sun, L.; Wang, L.; Tian, C.; Tan, T.; Xie, Y.; Shi, K.; Li, M.; Fu, H. Nitrogen-doped Graphene with High Nitrogen Level via a One-step Hydrothermal Reaction of Graphene Oxide with Urea for Superior Capacitive Energy Storage. *RSC Adv.* **2012**, *2*, 4498–4506.

(44) Wang, Y.; Shao, Y.; Matson, D. W.; Li, J.; Lin, Y. Nitrogen-Doped Graphene and Its Application in Electrochemical Biosensing. *ACS Nano* **2010**, *4*, 1790–1798.

(45) Qu, L.; Liu, Y.; Baek, J.-B.; Dai, L. Nitrogen-Doped Graphene as Efficient Metal-Free Electrocatalyst for Oxygen Reduction in Fuel Cells. *ACS Nano* **2010**, *4*, 1321–1326.

(46) Liu, J.; Zhao, Y.; Shi, L.; Yuan, S.; Fang, J.; Wang, Z.; Zhang, M. Solvothermal Synthesis of Crystalline Phase and Shape Controlled Sn⁴⁺-Doped TiO₂ Nanocrystals: Effects of Reaction Solvent. *ACS Appl. Mater. Interfaces* **2011**, *3*, 1261–1268.

(47) Södergren, S.; Siegbahn, H.; Rensmo, H.; Lindström, H.; Hagfeldt, A.; Lindquist, S.-E. Lithium Intercalation in Nanoporous Anatase TiO₂ Studied with XPS. *J. Phys. Chem. B* **1997**, *101*, 3087–3090.

(48) Xu, J.; Liu, X.; Chen, Y.; Zhou, Y.; Lu, T.; Tang, Y. Platinum–Cobalt Alloy Networks for Methanol Oxidation Electrocatalysis. *J. Mater. Chem.* **2012**, *22*, 23659–23667.

(49) Olsson, L.; Fridell, E. The Influence of Pt Oxide Formation and Pt Dispersion on the Reactions NO₂ ⇌ NO + 1/2 O₂ over Pt/Al₂O₃ and Pt/BaO/Al₂O₃. *J. Catal.* **2002**, *210*, 340–353.

(50) Schrauben, J. N.; Hayoun, R.; Valdez, C. N.; Braten, M.; Fridley, L.; Mayer, J. M. Titanium and Zinc Oxide Nanoparticles Are Proton-Coupled Electron Transfer Agents. *Science* **2012**, *336*, 1298–1301.

(51) Conesa, J. C.; Soria, J. Reversible Ti³⁺ Formation by H₂ Adsorption on M/TiO₂ Catalysts. *J. Phys. Chem.* **1982**, *86*, 1392–1395.

(52) Marken, F.; Bhambra, A. S.; Kim, D.-H.; Mortimer, R. J.; Stott, S. J. Electrochemical Reactivity of TiO₂ Nanoparticles Adsorbed onto Boron-Doped Diamond Surfaces. *Electrochem. Commun.* **2004**, *6*, 1153–1158.

(53) Di Valentin, C. D.; Pacchioni, G.; Selloni, A. Reduced and n-Type Doped TiO₂: Nature of Ti³⁺ Species. *J. Phys. Chem. C* **2009**, *113*, 20543–20552.

(54) Rothschild, A.; Komem, Y.; Levakov, A.; Ashkenasy, N.; Shapira, Y. Electronic and Transport Properties of Reduced and Oxidized Nanocrystalline TiO₂ Films. *Appl. Phys. Lett.* **2003**, *82*, 574–576.

(55) Ito, Y.; Cong, W.; Fujita, T.; Tang, Z.; Chen, M. High Catalytic Activity of Nitrogen and Sulfur Co-Doped Nanoporous Graphene in the Hydrogen Evolution Reaction. *Angew. Chem., Int. Ed.* **2015**, *54*, 2131–2136.